PHYSICAL REVIEW B **94**, 180402(R) (2016)

Temperature dependence of the magnon spin diffusion length and magnon spin conductivity in the magnetic insulator yttrium iron garnet

L. J. Cornelissen,[*] J. Shan, and B. J. van Wees
Physics of Nanodevices, Zernike Institute for Advanced Materials, University of Groningen,
Nijenborgh 4, 9747 AG Groningen, The Netherlands

(Received 5 July 2016; revised manuscript received 18 October 2016; published 4 November 2016)

We present a systematic study of the temperature dependence of diffusive magnon spin transport using nonlocal devices fabricated on a 210-nm yttrium iron garnet film on a gadolinium gallium garnet substrate. In our measurements, we detect spin signals arising from electrical and thermal magnon generation, and we directly extract the magnon spin diffusion length λ_m for temperatures from 2 to 293 K. Values of λ_m obtained from electrical and thermal generation agree within the experimental error with $\lambda_m = 9.6 \pm 0.9\ \mu$m at room temperature to a minimum of $\lambda_m = 5.5 \pm 0.7\ \mu$m at 30 K. Using a two-dimensional finite element model to fit the data obtained for electrical magnon generation we extract the magnon spin conductivity σ_m as a function of temperature, which is reduced from $\sigma_m = 3.7 \pm 0.3 \times 10^5$ S/m at room temperature to $\sigma_m = 0.9 \pm 0.6 \times 10^4$ S/m at 5 K. Finally, we observe an enhancement of the signal originating from thermally generated magnons for low temperatures where a maximum is observed around $T = 7$ K. An explanation for this low-temperature enhancement is however still missing and requires additional investigation.

DOI: 10.1103/PhysRevB.94.180402

Magnons, the quanta of spin waves, can be excited in magnetic insulators in various ways: magnetically via microwave-frequency ac currents [1], thermally via the spin Seebeck effect (SSE) [2], or electrically via low-frequency or dc electric currents making use of the interfacial spin-flip scattering mechanism. The latter excitation method has attracted a lot of attention recently, both experimentally [3–8] and theoretically [9–12]. It relies on the exchange coupling between the spin accumulation in a normal metal (NM) and the magnons in a magnetic insulator (MI) where the materials of choice are typically platinum (Pt) for the NM and yttrium iron garnet (YIG) as the MI. Via this exchange coupling, the spin current can be transferred between the MI and the NM. The spins in the MI are then carried by magnons and transported diffusively, allowing for the definition of a magnon spin diffusion length (λ_m) and a magnon spin conductivity (σ_m) analogous to their counterparts in diffusive electron spin transport [12]. Several recent experiments investigated the temperature dependence of diffusive magnon spin currents [4–7], and a systematic study of λ_m and σ_m as a function of temperature is carried out here. Recently, the relevant length scale for the local SSE was measured as a function of temperature [13] which as we show here exhibits a different temperature dependence than λ_m. Additionally, Giles *et al.* extracted λ_m using experiments where magnons are generated via laser heating and found $47 \leqslant \lambda_m \leqslant 73\ \mu$m at 23 K [14] and an upper bound of $\lambda_m \leqslant 10\ \mu$m at 280 K. However, they did not report the full temperature dependence of λ_m, which we do identify here. Furthermore, Kehlberger *et al.* [15] reported the relevant length scale for the local SSE for YIG samples grown by pulsed laser deposition (PLD) and liquid phase epitaxy (LPE). They found a length scale on the order of 100 nm for PLD YIG at room temperature, 1 μm for LPE YIG at room temperature, and 7 μm for LPE YIG at 50 K. Finally, Wu *et al.* [7] reported a spin diffusion length of 38 nm for sputtered YIG at room temperature using a measurement scheme similar to what we employ here but in a Pt|YIG|Pt sandwich rather than lateral geometry.

In this Rapid Communication we investigate the diffusive transport of magnon spins as a function of sample temperature. We employ the nonlocal measurement geometry that was developed in our earlier work [3] in which we measure the magnon spin signal as a function of distance, which allows us to directly extract λ_m for temperatures from 2 to 293 K. In this measurement scheme, magnon injection and detection results from the exchange interaction between a spin accumulation in the platinum injector and detector (created and probed by the spin Hall and inverse spin Hall effect, respectively) and magnons in the YIG. This implies that the distance over which the magnon spin current diffuses is well defined since the locations of both magnon injection and detection are strictly determined, allowing us to unambiguously extract the magnon spin diffusion length [8]. Additionally, we use a two-dimensional (2D) finite element model (FEM) to describe the magnon transport in our devices [12], which enables us to determine σ_m as a function of temperature.

A microscope image of a typical device is shown in the inset of Fig. 1. The devices consist of two parallel platinum strips on top of a YIG thin film, separated by a distance d from each other and contacted by Ti/Au leads. The YIG film thickness is $t = 210$ nm, and it was grown by liquid phase epitaxy in the [111] direction on top of a 500-μm-thick gadolinium gallium garnet ($Gd_3Ga_5O_{12}$, GGG) substrate. YIG|GGG samples were obtained commercially from Matesy GmbH. Three steps of electron-beam (e-beam) lithography were used to define the devices on top of the YIG film. In the first step we define a pattern of Ti/Au markers (deposited by e-beam evaporation), used to align the subsequent steps. Injectors and detectors are defined in the second step where approximately 10 nm of platinum are deposited using magnetron sputtering in an Ar^+ plasma. Finally, we define Ti/Au (5/75-nm) leads and bonding pads using e-beam evaporation. Prior to Ti evaporation, we perform argon-ion milling to remove any polymer residues

---

[*] l.j.cornelissen@rug.nl

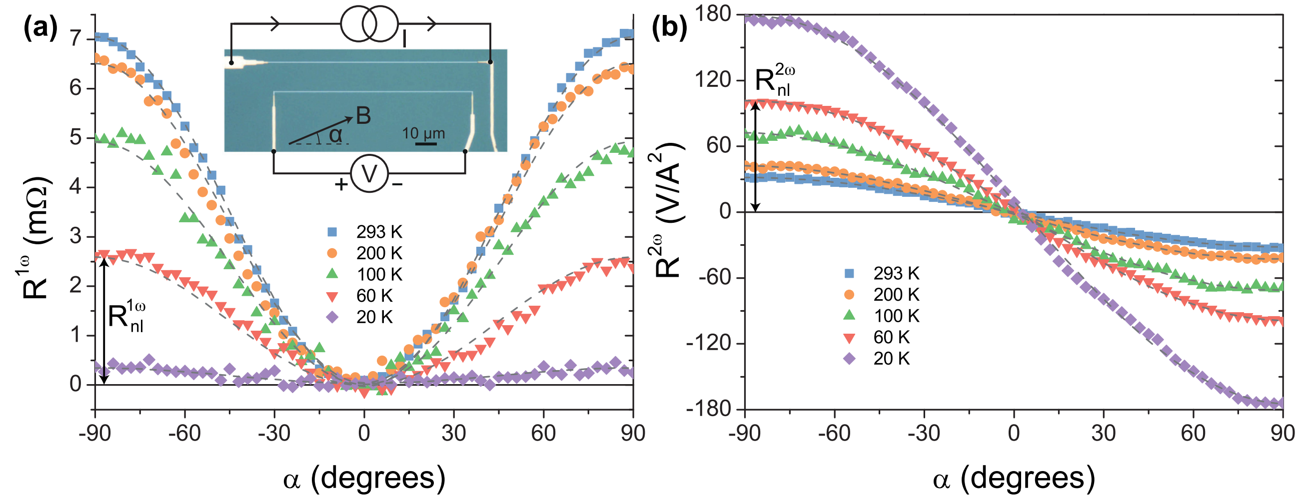

FIG. 1. Nonlocal signals as a function of angle α between the magnetic-field B and the injector/detector strips for an injector-detector separation distance of $d = 3.5\ \mu$m and various sample temperatures. The inset shows an optical microscope image of one of the devices with current and voltage connections indicated schematically. (a) First-harmonic signal. The dashed lines are $\sin^2(\alpha)$ fits through the data. (b) Second-harmonic signal. The dashed lines are $\sin(\alpha)$ fits through the data. The amplitudes of the nonlocal signasl $R^{1\omega}_{\mathrm{nl}}$ and $R^{2\omega}_{\mathrm{nl}}$ are indicated in (a) and (b), respectively, for $T = 60$ K. The sign convention is the same as in Ref. [3], meaning that a positive $R^{2\omega}_{\mathrm{nl}}$ implies a second-harmonic voltage that is *opposite* to what would be obtained for a local current-driven spin Seebeck measurement.

from the Pt strips. Length and width of the platinum strips are approximately $L = 100\ \mu$m and $w = 300$ nm for all devices.

Nonlocal measurements are performed by applying an ac charge current I to the injector at a frequency ω [typically $I_{\mathrm{rms}} = 100\ \mu$A and $\omega/(2\pi) = 3.423$ Hz]. This current generates magnons in the YIG via two different mechanisms: Due to the spin Hall effect, a transverse spin current is generated towards the YIG, and a spin accumulation μ_s builds up at the Pt|YIG interface. Via the exchange interaction at the interface, μ_s generates a magnon spin accumulation μ_m in the YIG. This is a fully linear process, i.e., $\mu_m \propto I$. Additionally, heat is generated in the injector via Joule heating, which induces a temperature gradient ∇T in the YIG. By virtue of the spin Seebeck effect, this gradient causes a magnon spin current to flow. The spin current $\mathbf{j}_m$ is linear with the temperature gradient, which in turn is proportional to the current *squared*, i.e., $\mathbf{j}_m \propto \nabla T \propto I^2$. At the detector interface, magnon spins in the YIG are converted into a spin accumulation in the Pt, which is then converted to a charge voltage V via the inverse spin Hall effect. Note that a finite ∇T is likely present close to the *detector* as well, which also generates a magnon spin current that can give rise to a second-harmonic signal. However, due to the different characteristic decays of the heat and spin current with distance (algebraic compared to exponential decay, respectively, in the regime where $d > \lambda_m, t$ [12]), we can verify that magnons which are generated near the *injector* and then diffuse to the detector dominate the second-harmonic signal in our devices.

Using a lock-in detection technique [16] we can detect signals due to processes that are linear and quadratic in the current separately. The nonlocal first-harmonic signal is then given by $R^{1\omega} = V^{1\omega}/I$ (due to electrical generation), whereas the second-harmonic signal is $R^{2\omega} = V^{2\omega}/I^2$ (thermal generation). In the nonlocal measurements we are thus sensitive to the generation, transport, and detection of magnons where the only difference between the first and the second harmonics lies in the generation process.

We now rotate the sample in an external in-plane magnetic field large enough to align the YIG magnetization $\mathbf{M}$ ($B =$ 10 mT) thus varying angle α between $\mathbf{M}$ and the Pt strips. For electrical generation of magnons, both the injection and the detection processes depend on the projection of $\mathbf{M}$ on the spin accumulation in the Pt, which leads to $R^{1\omega} = R^{1\omega}_{\mathrm{nl}} \sin^2(\alpha)$ for the first-harmonic signal as can be seen in Fig. 1(a). For thermally generated magnons, only the detection depends on α, resulting in $R^{2\omega} = R^{2\omega}_{\mathrm{nl}} \sin(\alpha)$ for the second-harmonic signal as can be observed in Fig. 1(b). The first-harmonic signal decreases for decreasing sample temperature, which is consistent with previous observations [4–6] and theoretical predictions [10,12,17]. Interestingly, the second-harmonic signal shows the opposite trend and significantly increases as T is reduced.

By performing measurements for various injector-detector separation distances d, we extract the signal amplitude as a function of distance. The results are shown in Fig. 2(a) for the first-harmonic signal and Fig. 2(b) for the second-harmonic signal for several temperatures. For long distances, the decay of the magnon spin signal is governed by the magnon spin diffusion length λ_m. As we showed in Ref. [3], λ_m can be extracted from both the first- and the second-harmonic signals by fitting the distance-dependent data [18] to the one-dimensional magnon spin diffusion model,

$$R_{\mathrm{nl}}(d) = \frac{A}{\lambda_m} \frac{\exp(d/\lambda_m)}{1 - \exp(2d/\lambda_m)}, \tag{1}$$

where A is a prefactor that depends for instance on the efficiency of the magnon injection (governed by the effective spin conductance g_s [12]) and on the magnon diffusion constant. The model in Eq. (1) assumes transparent injector and detector contacts, a condition that even at room temperature is not completely fulfilled due to the finite value of g_s.

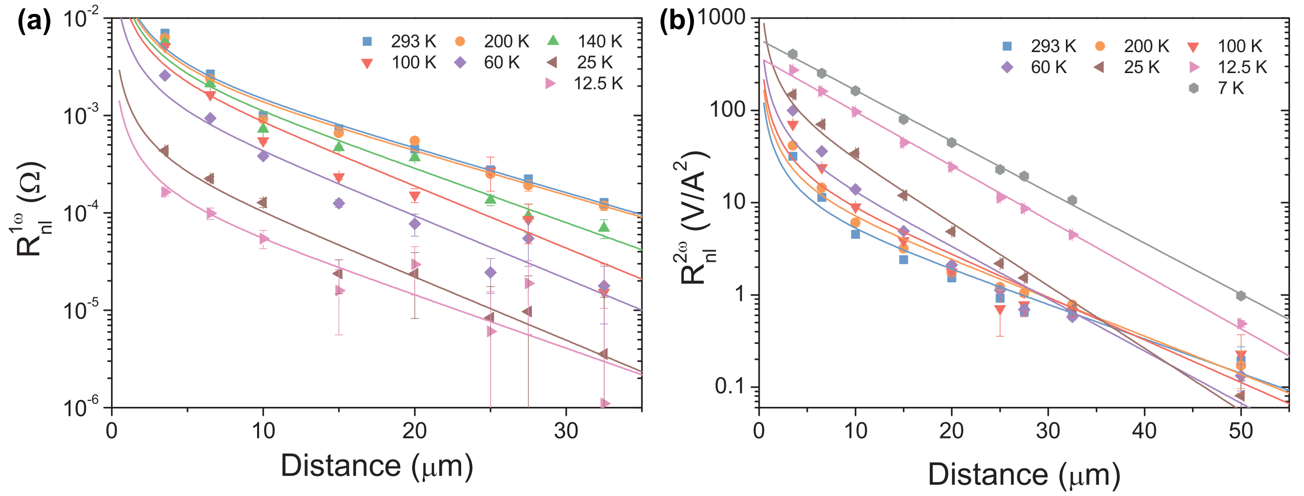

FIG. 2. Distance dependence of the amplitudes of the nonlocal (a) first- and (b) second-harmonic signals. Error bars indicate one standard error of the amplitude obtained from the fits to the angle-dependent data. The solid lines are fits of the data to Eq. (1). Exceptions to this are the solid lines in the low-temperature ($T \leqslant 12.5$-K) second-harmonic data, which are better described by a pure exponential fit.

Additionally, g_s scales as $g_s \propto (\frac{T}{T_C})^{3/2}$ [12,17] so that for $T \rightarrow 0$ the interfaces become increasingly opaque, making the applicability of the model questionable for low temperatures. However, we can still use the model to determine λ_m since that is only determined by the decay of the signal in the long-distance regime (i.e., the slope of the curves in Fig. 2 for distances of $d > 10$ μm). For $T < 25$ K the signal-to-noise ratio (SNR) in the first harmonic is $\ll 1$ for devices with $d > 10$ μm such that we can no longer reliably extract λ_m.

The distance dependence of the second harmonic is generally more complicated than that of the first harmonic due to the delocalized nature of thermal magnon generation, even showing a sign change for very short distances ($d \leqslant 200$ nm) as we showed in Ref. [3]. However, for distances longer than the magnon spin diffusion length we can still use the model in Eq. (1) to extract λ_m from the second-harmonic data. We stress that the exponential decay in this regime can only be explained by magnons being generated thermally in close vicinity of the injector, which then diffuse to the detector. Interestingly, for $T < 25$ K the second-harmonic distance dependence shows almost pure exponential decay described by

$$R_{\mathrm{nl}}^{2\omega} = B \exp\left(-d/\lambda_m^{2\omega}\right), \tag{2}$$

over approximately three orders of magnitude. In this regime we thus extract $\lambda_m^{2\omega}$ by fitting the data to Eq. (2). This crossover to a pure exponential might be explained by the reduction of interface transparency due to the decrease in g_s. This can also be observed in spin transport in metallic nonlocal spin valves where transparent contacts result in signal decay similar to our Eq. (1), but opaque contacts yield pure exponential decay [19].

Figure 3 shows the magnon spin diffusion length $\lambda_m^{1\omega}$ ($\lambda_m^{2\omega}$) that we found from the first- (second-) harmonic signals as a function of temperature. It can be seen that $\lambda_m^{1\omega}$ and $\lambda_m^{2\omega}$ approximately agree within the experimental error, which further supports our claim that there is no difference in the transport mechanism for electrically and thermally excited magnons. Furthermore, there is only a small change in λ_m over the probed temperature range. Since $\lambda_m = v_{\mathrm{th}}\sqrt{\frac{2}{3}\tau\tau_{\mathrm{mr}}}$ [12] with v_{th} as the magnon thermal velocity, τ as the momentum relaxation time, and τ_{mr} as the magnon spin-relaxation time, we attribute this to the fact that, although the relaxation times increase as T decreases, this is compensated by the reduction in thermal velocity of the magnons. Our results differ significantly from the findings of Giles *et al.* [14], who reported as a lower bound $\lambda_m = 43$ μm at 23 K [compared to $\lambda_m(T = 25) = 6.7 \pm 0.6$ μm that we find here). Note that we study a 210-nm-thin YIG film on a GGG substrate, whereas Giles *et al.* [14] studied a 0.5-mm-thick YIG substrate.

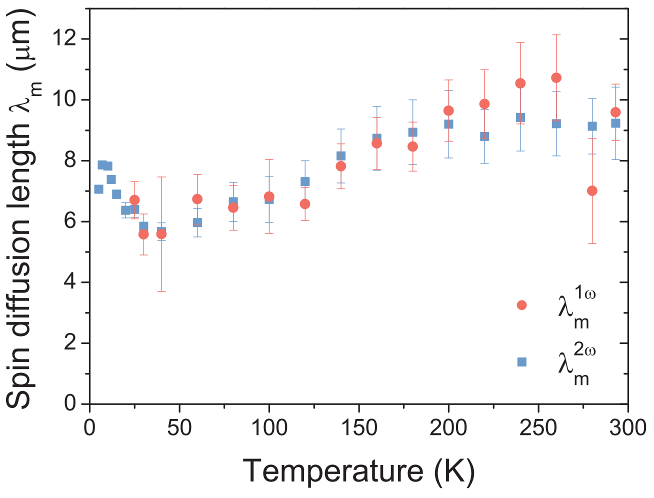

FIG. 3. Magnon spin diffusion length as a function of temperature, obtained from the distance dependence of the first-harmonic ($\lambda_m^{1\omega}$) and second-harmonic ($\lambda_m^{2\omega}$) signals. λ_m was extracted by fitting the data to Eq. (1). Error bars indicate one standard error obtained from the fits. For $T \geqslant 25$ K, $\lambda_m^{1\omega}$ and $\lambda_m^{2\omega}$ agree within the experimental uncertainties. For $T < 25$ K, the SNR in the first harmonic is $\ll 1$ for distances of $d > 10$ μm, making reliable extraction of $\lambda_m^{1\omega}$ impossible. However, due to the increase in the second-harmonic signal for decreasing temperature, $\lambda_m^{2\omega}$ can be extracted very accurately in this regime, explaining the small error bars on $\lambda_m^{2\omega}$ here.

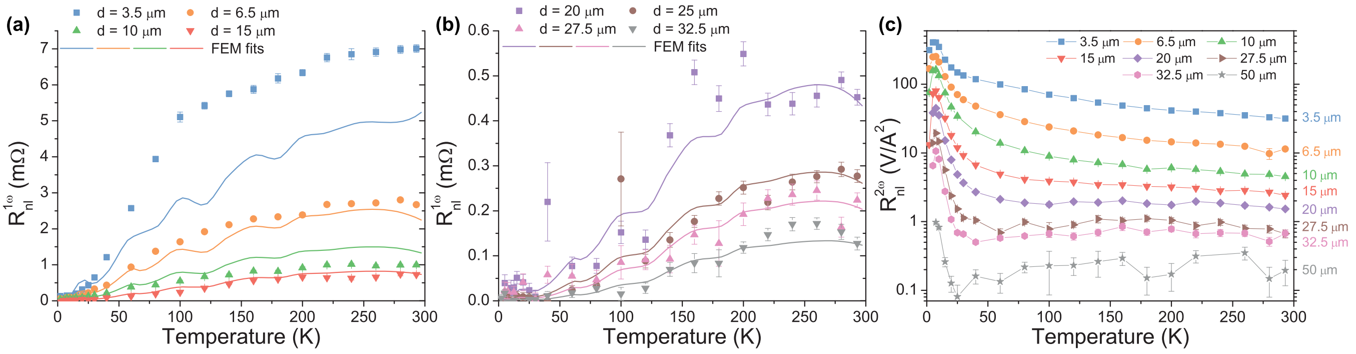

FIG. 4. Replot of the data already partially shown in Fig. 2 now as a function of temperature. (a) and (b) Amplitudes of the first-harmonic nonlocal resistance (symbols) for various injector-detector distances as a function of temperature. The solid lines show the results of the temperature-dependent 2D FEM for every distance. In the FEM, σ_m is used as the only free parameter to fit the data from all distances at each measured temperature with intervals of $\Delta T = 20$ K. The fit results are then interpolated to obtain the solid lines shown here. The structure that can be seen in these lines results from our finite sampling intervals. (c) Amplitude of the second-harmonic nonlocal resistance for various distances as a function of temperature on a logarithmic scale. The signal peaks at $T \approx 7$ K for all distances.

However, recent magnon spin transport studies in our group did not show significant variation in λ_m for YIG film thicknesses up to 50 μm at room temperature [20].

Our observed $\lambda_m(T)$ also differs from recent experiments which rely on the YIG thickness dependence of the local SSE to determine the propagation length ξ of thermally excited magnons [13]. The authors of Ref. [13] found a scaling of $\xi \propto T^{-1}$. These different observations show that it is crucial to investigate the relevant length scale in both local and nonlocal geometries in order to develop a complete physical picture of the SSE.

Focusing on the electrical generation of magnons, we use the 2D finite element model which we developed in Ref. [12] to describe the first-harmonic nonlocal resistance as a function of temperature. The model, which is based on the linear-response transport theory for the diffusive spin and heat transport of magnons, is described in detail in Ref. [12]. Magnon spin transport in the bulk of the YIG (in corresponding electrical units) is described by

$$\frac{2e}{\hbar}\mathbf{j}_m = -\sigma_m \nabla \mu_m, \tag{3}$$

$$\nabla^2 \mu_m = \frac{\mu_m}{\lambda_m^2}, \tag{4}$$

where $\mathbf{j}_m$ is the magnon spin current, e is the electron charge, $\hbar$ is the reduced Planck constant, σ_m is the magnon spin conductivity, μ_m is the magnon chemical potential, and λ_m is the magnon spin diffusion length. Spin currents across the Pt|YIG interface are given by $j_m^{\text{int}} = g_s(\mu_s - \mu_m)$, where μ_s is the spin accumulation at the Pt side of the interface and μ_m is the magnon chemical potential on the YIG side. In linear response, magnon spin transport in our Pt|YIG devices is thus governed by three parameters: λ_m, σ_m, and g_s. We employ a zero perpendicular spin current boundary condition at the YIG|GGG interface since, although a paramagnetic spin Seebeck effect has been observed in GGG at low temperatures [21], this effect only contributes at magnetic fields much larger than our typical external field. Therefore, for the low fields we are using we can safely assume that no magnon spin currents leak away into the GGG.

Using our model, we aim to find $\sigma_m(T)$ which is thus treated as the only fit parameter. $\lambda_m(T)$ is found from the distance dependence of the nonlocal signals directly as shown in Fig. 3, and we use $g_s(T) = g_s(293)(T/293)^{3/2}$, where $g_s(293)$ is the value for g_s at room temperature (293 K). We extracted $G_r = 2.5 \times 10^{14}$ S/m^2 from spin Hall magnetoresistance measurements [22,23] of our devices at room temperature from which we obtain $g_s(293) = 1.5 \times 10^{13}$ S/m^2, comparable to what we found for our previous devices in Refs. [3,12]. Furthermore, the spin accumulation generated at the interface of the Pt injector and the YIG was calculated using $\mu_s = 2\theta_{\text{SH}} j_c \frac{\lambda_s}{\sigma_e} \tanh\left(\frac{t}{2\lambda_s}\right)$ [24,25], where θ_{SH} is the spin Hall angle in Pt, j_c is the charge current density in the injector, λ_s is the spin diffusion length in Pt, σ_e is the Pt conductivity, and t is the Pt thickness. $\sigma_e(T)$ is extracted independently from resistivity measurements on the injector strips and used as input in the FEM. Furthermore, the temperature dependence of λ_s was included using interpolation of the data reported in Ref. [26]. Finally, the nonlocal signal is found by calculating the average spin current density $\langle j_s \rangle$ in the detector, which is then converted to nonlocal resistance using $R_{\text{nl}} = \theta_{\text{SH}} L \langle j_s \rangle / (I \sigma_e)$.

Figure 4 shows the measured first-harmonic nonlocal resistance as a function of temperature for various distances. The solid lines are the results of the fit of the FEM to the experimental data with σ_m as the only free parameter. Fits are performed to data for all distances at each measured temperature to extract $\sigma_m(T)$ [27]. The agreement between model and experiment is reasonable as the model is generally less than a factor of 2 off, even for $d = 3.5$ μm where the largest discrepancy is observed.

The resulting temperature dependence $\sigma_m(T)$ is shown in Fig. 5 where the error bars indicate one standard error in σ_m obtained from the fits. Note that the value we find for σ_m at room temperature $\sigma_m(293) = 3.7 \pm 0.3 \times 10^5$ S/m is comparable to $\sigma_m = 5 \times 10^5$ S/m, which we extracted previously from an independent set of data obtained from different devices (the majority of which were fabricated on samples cut from the same YIG|GGG wafer) [12].

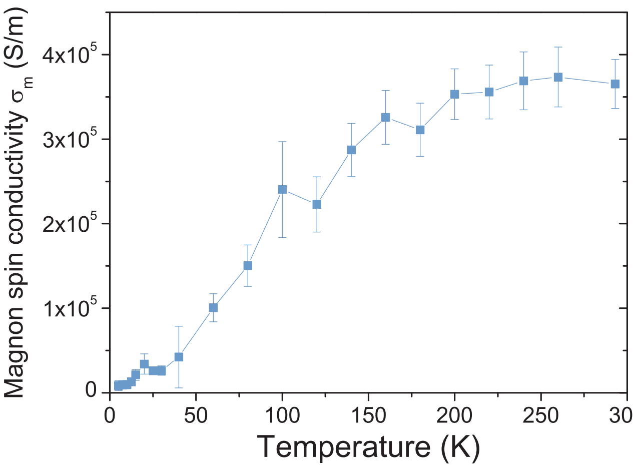

FIG. 5. Magnon spin conductivity $\sigma_m(T)$ as a function of sample temperature, extracted from least-squares fits of the 2D FEM to the experimental first-harmonic data [Figs. 4(a) and 4(b)]. The FEM is used to fit the distance dependence of the signal at each temperature with $\sigma_m(T)$ as the only free parameter. Error bars indicate one standard error obtained from the fits.

Figure 4(c) shows that the second-harmonic signal exhibits a maximum at $T \approx 7$ K for all distances. Below 7 K the signals decrease again, even changing sign for long distances ($d \geqslant 20$ μm) [28]. This sign change is not well understood and calls for further investigation. In particular, a study of the nonlocal second-harmonic signal temperature dependence as a function of YIG thickness may lead to more insight in the complicated generation mechanism for thermal magnon excitation since recent experimental results show that the distance at which the sign change occurs (at room temperature) depends on the thickness of the YIG film whereas λ_m does not depend on film thickness [20].

The enhancement in the second-harmonic signal is at present not well understood. However, we do attribute it to an enhancement in thermal magnon generation at or close to the injector (rather than changes in the transport or detection of the magnons) since the only difference between the first- and the second-harmonic signals lies in the generation mechanism of the magnons. This could mean that the spin Seebeck coefficient in the YIG is enhanced for decreasing temperature, however an extensive analysis is needed to draw further conclusions regarding the origin of this enhancement. Since we focused here on the temperature dependence of the transport parameters involved, we leave this analysis for future work.

In conclusion, we report the temperature dependence of the magnon spin diffusion length and the magnon spin conductivity in the YIG, which we extracted from nonlocal magnon spin transport measurements. We observe only a slight change in λ_m with temperature, which we attribute to the fact that the increase in magnon relaxation time is compensated by the reduced thermal velocity of the magnons. The close agreement in λ_m for electrically injected and thermally generated magnons confirms that the same (exchange) magnons are involved and supports the description of the nonequilibrium transport in terms of a magnon chemical potential [12]. For electrically generated magnons, we modeled the distance and temperature dependence of the nonlocal signal quantitatively using a 2D finite element model which was developed in earlier work. The model gives good agreement with the experimental observations over the whole temperature range and allowed us to find the temperature dependence of σ_m, which we find to decrease by roughly an order of magnitude from room temperature to $T = 5$ K. For thermally generated magnons, we observe that the nonlocal signal increases with decreasing temperature and peaks around $T \approx 7$ K. Additional experimental and theoretical studies are required to understand this enhancement.

The authors would like to acknowledge H. M. de Roosz, J. G. Holstein, H. Adema, and T. J. Schouten for technical assistance. This work is part of the research program of the Foundation for Fundamental Research on Matter (FOM) and supported by NanoLab NL, EU FP7 ICT Grant No. 612759, InSpin, and the Zernike Institute for Advanced Materials.

---

[1] A. V. Chumak, V. I. Vasyuchka, A. A. Serga, and B. Hillebrands, Nat. Phys. **11**, 453 (2015).

[2] K. Uchida, J. Xiao, H. Adachi, J. Ohe, S. Takahashi, J. Ieda, T. Ota, Y. Kajiwara, H. Umezawa, H. Kawai, G. E. W. Bauer, S. Maekawa, and E. Saitoh, Nat. Mater. **9**, 894 (2010).

[3] L. J. Cornelissen, J. Liu, R. A. Duine, J. B. Youssef, and B. J. van Wees, Nat. Phys. **11**, 1022 (2015).

[4] S. T. B. Goennenwein, R. Schlitz, M. Pernpeintner, K. Ganzhorn, M. Althammer, R. Gross, and H. Huebl, Appl. Phys. Lett. **107**, 172405 (2015).

[5] S. Vélez, A. Bedoya-Pinto, W. Yan, L. E. Hueso, and F. Casanova, arXiv:1606.02968.

[6] J. Li, Y. Xu, M. Aldosary, C. Tang, Z. Lin, S. Zhang, R. Lake, and J. Shi, Nat. Commun. **7**, 10858 (2016).

[7] H. Wu, C. H. Wan, X. Zhang, Z. H. Yuan, Q. T. Zhang, J. Y. Qin, H. X. Wei, X. F. Han, and S. Zhang, Phys. Rev. B **93**, 060403 (2016).

[8] L. J. Cornelissen and B. J. van Wees, Phys. Rev. B **93**, 020403(R) (2016).

[9] J. Xiao and G. E. W. Bauer, arXiv:1508.02486.

[10] S. S.-L. Zhang and S. Zhang, Phys. Rev. B **86**, 214424 (2012).

[11] S. S.-L. Zhang and S. Zhang, Phys. Rev. Lett. **109**, 096603 (2012).

[12] L. J. Cornelissen, K. J. H. Peters, G. E. W. Bauer, R. A. Duine, and B. J. van Wees, Phys. Rev. B **94**, 014412 (2016).

[13] E.-J. Guo, J. Cramer, A. Kehlberger, C. A. Ferguson, D. A. MacLaren, G. Jakob, and M. Kläui, Phys. Rev. X **6**, 031012 (2016).

[14] B. L. Giles, Z. Yang, J. S. Jamison, and R. C. Myers, Phys. Rev. B **92**, 224415 (2015).

[15] A. Kehlberger, U. Ritzmann, D. Hinzke, E.-J. Guo, J. Cramer, G. Jakob, M. C. Onbasli, D. H. Kim, C. A. Ross, M. B. Jungfleisch, B. Hillebrands, U. Nowak, and M. Kläui, Phys. Rev. Lett. **115**, 096602 (2015).

[16] N. Vlietstra, J. Shan, B. J. van Wees, M. Isasa, F. Casanova, and J. Ben Youssef, Phys. Rev. B **90**, 174436 (2014).

[17] S. A. Bender, R. A. Duine, and Y. Tserkovnyak, Phys. Rev. Lett. **108**, 246601 (2012).

[18] To ensure that data from all distances are weighed equally, we perform the fit on $\log_{10}$ of the data using also $\log_{10}$ of Eq. (1) as a fitting function.

[19] S. Takahashi and S. Maekawa, Phys. Rev. B **67**, 052409 (2003).

[20] J. Shan, L. J. Cornelissen, N. Vlietstra, J. Ben Youssef, T. Kuschel, R. A. Duine, and B. J. van Wees, arXiv:1608.01178.

[21] S. M. Wu, J. E. Pearson, and A. Bhattacharya, Phys. Rev. Lett. **114**, 186602 (2015).

[22] H. Nakayama, M. Althammer, Y.-T. Chen, K. Uchida, Y. Kajiwara, D. Kikuchi, T. Ohtani, S. Geprägs, M. Opel, S. Takahashi, R. Gross, G. E. W. Bauer, S. T. B. Goennenwein, and E. Saitoh, Phys. Rev. Lett. **110**, 206601 (2013).

[23] N. Vlietstra, J. Shan, V. Castel, B. J. van Wees, and J. Ben Youssef, Phys. Rev. B **87**, 184421 (2013).

[24] J. Flipse, F. K. Dejene, D. Wagenaar, G. E. W. Bauer, J. B. Youssef, and B. J. van Wees, Phys. Rev. Lett. **113**, 027601 (2014).

[25] M. Schreier, A. Kamra, M. Weiler, J. Xiao, G. E. W. Bauer, R. Gross, and S. T. B. Goennenwein, Phys. Rev. B **88**, 094410 (2013).

[26] M. Isasa, E. Villamor, L. E. Hueso, M. Gradhand, and F. Casanova, Phys. Rev. B **91**, 024402 (2015).

[27] We again fit $\log_{10}$ of the data to $\log_{10}$ of the model outcome to obtain equal weighting for data from all distances.

[28] Data points with negative amplitudes are not visible in Fig. 4(c) due to the logarithmic scale of the plot. The sign changes occur in the region of $2 < T < 5$ K, depending on the distance.